

The origin of the ferroelectric-like orthorhombic phase in oxygen-deficient HfO_{2-y} nanoparticles

Eugene A. Eliseev,^{1*} Iryna V. Kondakova¹, Yuri O. Zagorodniy,¹ Hanna V. Shevilakova,² Oksana V. Leshchenko,¹ Victor N. Pavlikov,¹ Lesya P. Yurchenko,¹ Myroslav V. Karpets,¹ and Anna N. Morozovska^{3†}

¹Frantsevich Institute for Problems in Materials Science, National Academy of Sciences of Ukraine
Kyiv, Ukraine

²Department of Microelectronics Igor Sikorsky Kyiv Polytechnic Institute Kyiv, Ukraine

³Institute of Physics National Academy of Sciences of Ukraine Kyiv, Ukraine

Abstract

In this work we established the relationship between the crystalline structure symmetry, point defects and possible appearance of the ferroelectric-like polarization in HfO_{2-y} nanoparticles. Notably, that XRD and EPR analysis revealed the formation of the ferroelectric-like orthorhombic phase in the oxygen-deficient HfO_{2-y} nanoparticles (pure and doped with rare-earth element yttrium). DFT calculations showed that small HfO_2 nanoparticles may become polar, especially in the presence of impurity atoms and/or oxygen vacancies. To explain the experimental results, we have modified the effective LGD model through the parameterization approach, focusing on the Landau expansion coefficients associated with the polar (FE) and antipolar (AFE) orderings, which agrees with the performed DFT calculations. The effective LGD model can be useful for the development of the novel generation of silicon-compatible ferroelectric nanomaterials based on the $\text{Hf}_x\text{Zr}_{1-x}\text{O}_{2-y}$.

Keywords — nanoparticles, hafnia oxide, oxygen vacancies, rare-earth element doping, ferroelectric-like polar phase

* Corresponding author: eugene.a.eliseev@gmail.com

† Corresponding author: anna.n.morozovska@gmail.com

INTRODUCTION

The discovery of ferroelectric and antiferroelectric properties in thin films of lead-free hafnium (HfO_2) and zirconium (ZrO_2) oxides open them for next-generation of Si-compatible ferroelectric memory elements like ferroelectric random-access memories (FeRAMs) and field-effect transistors (FETs) [1, 2]. However, a comprehensive understanding of the crucial interplay between stoichiometry, oxygen vacancies, size, and surface effects in nanosized $\text{Hf}_x\text{Zr}_{1-x}\text{O}_{2-y}$ remains elusive still [3].

Bulk HfO_2 and ZrO_2 , characterized as high-k dielectrics, lack inherent ferroelectric properties across a wide range of standard temperatures and pressures [4, 5]. This behavior undergoes a dramatic shift when these materials are scaled down to the nanoscale, where complex interactions and structural transitions come into play. One key factor influencing the observed ferroelectric properties in $\text{Hf}_x\text{Zr}_{1-x}\text{O}_2$ films is the presence of the polar orthorhombic phase. However, this phase suffers from metastability compared to the bulk monoclinic phase, leading to challenges with ferroelectric phase stability. Additionally, the properties of these thin films are highly sensitive to various factors, including substrate material, annealing conditions, deposition method, film thickness, and dopant concentrations [6, 7, 8]. Depending on the interplay of these factors, the value of x in $\text{Hf}_{1-x}\text{Zr}_x\text{O}_2$ films can range from 0 to 1, ultimately dictating whether the material exhibits dielectric, ferroelectric, or antiferroelectric behavior [9, 10].

Extensive theoretical [11, 12, 13] and experimental [14, 15, 16] theoretical and experimental evidence, as highlighted in our previous studies [29, 30, 31], underscores the critical role of surface and grain boundary energy, alongside oxygen vacancies, in optimizing these materials for practical applications in advanced FeRAM and FET technologies. Further research and optimization efforts are still required to fully unlock the full potential of binary oxide $\text{Hf}_x\text{Zr}_{1-x}\text{O}_{2-y}$ nanoparticles (see **Table I**).

Table I. Properties of $\text{Hf}_x\text{Zr}_{1-x}\text{O}_{2-y}$ nanoparticles and thin films (for comparison)

Material	Doping	Geometry	Size/thickness (nm)	Symmetry group(s)	Ferroelectric properties	Synthesis method	Ref.
$\text{Hf}_x\text{Zr}_{1-x}\text{O}_2$	None	Particles of faceted shape	5.5, 4.3, 3.6	tetragonal or cubic	n/m	Sol-gel	¹⁷
HfO_2	None	particle	10 - 15	monoclinic phase ($P2_1/c$)	n/m	auto-igniting combustion	¹⁸
HfO_2	None	spherical particles	8.79, 7.16, 6.78	monoclinic	n/m	precipitation method	¹⁹
HfO_2	None	particle	4 - 120	Tetragonal and monoclinic	n/m	hydrothermal route	²⁰

HfO ₂	None	particle	61 - 80	n/m	low loss dielectric composite	US Research Nanomaterials, Inc.	21
HfO ₂	None	particle	60 – 90	monoclinic	n/m	hydrothermal synthesis	22
HfO ₂	Dy and Sm co-doped	particle	10 - 31	monoclinic and cubic phases	n/m	Pechini type sol-gel method	23
Hf _x Zr _{1-x} O _{2-y}	O-vacancies	particle	n/m	m o + m	possible from XRD Yes (theory)	Organo-nitrate; pyrogenic	24
HfO ₂	either Eu ³⁺ or Nb ⁵⁺ doping	particle	17 - 47	monoclinic + small amount of tetragonal phase	n/m	Sol-Gel and Combustion Synthesis	25
Hf _{0.5} Zr _{0.5} O ₂	None	Particles of spindle-like or spherical shape	200 - 50 3 – 4	orthorhombic <i>Pca</i> ₂₁ <i>Pbca</i> , <i>Pbcm</i>	possible from XRD	Hydro-thermal synthesis from HfCl ₄ and ZrCl ₄	26
HfO ₂	Si-, Al-, Gd-doped	film	10 nm and 40 nm thick	Orthorhombic (<i>Pca</i> ₂₁)	polarization hysteresis in electric field	atomic layer deposition (ALD)	27
Hf _{0.5} Zr _{0.5} O ₂	None O-deficient (air, high-vacuum, Ar)	film	17 nm	orthorhombic /tetragonal	Yes (PFM response hysteresis loop)	plasma-enhanced ALD	28

This work aims to bridge this gap by investigating the charge-polarization coupling within these materials using the Landau-Ginzburg-Devonshire (LGD) model [29, 30, 31] in complex with DFT calculations, which allows to determine the "effective" Landau expansion coefficients for polar (FE) and antipolar (AFE) orderings in hafnia-based compounds. To verify the effectiveness of the LGD model, we explain the X-ray diffraction and EPR data for oxygen-deficient HfO_{2-y} nanoparticles to determine their phase composition, as well as the nanoparticles prepared under varying annealing conditions (pure and doped with yttrium Y) and explain the formation of the ferroelectric-like orthorhombic phase in them.

THEORETICAL DESCRIPTION

A. “Effective” Landau-Ginzburg-Devonshire model

Further analysis of the spatial-temporal evolution of polarization in the nanosized Hf_xZr_{1-x}O_{2-y} is conducted using a combined approach. This approach incorporates elements of the Kittel-type model [32], incorporating both polar and antipolar modes [33, 34, 35], with the theoretical framework of the Landau-Ginzburg-Devonshire (LGD) approach [29, 30, 31]. Within this framework, the free energy functional F is expressed as the sum of several key terms [29 - 31]:

$$F = F_{bulk} + F_{grad} + F_{el} + F_S. \quad (1)$$

The first term represents the bulk free energy, an expansion based on the second and fourth powers of both the polar (P_f) and antipolar (A_f) order parameters, F_{bulk} :

$$F_{bulk} = \int_{V_f} d^3r \left(\frac{a_P}{2} P_f^2 + \frac{b_P}{4} P_f^4 + \frac{\eta}{2} P_f^2 A_f^2 + \frac{a_A}{2} A_f^2 + \frac{b_A}{4} A_f^4 \right). \quad (2a)$$

Here V_f is the volume and surface area of the HfO_{2-y} nanoparticle. Subsequent terms account for the energy contribution arising from gradients in the polarization (F_{grad}), the electrostatic energy (F_{el}), and the surface energy (F_S), respectively are listed in Refs.[29 - 31].

It is important to consider how the LGD expansion coefficients depend on various factors, which in turn can be influenced by temperature, size, elastic stresses and/or strains. For classical ferroelectric films with a pronounced temperature-dependent and strain-dependent soft mode, the coefficients a_P and a_A exhibit a linear relationship with both temperature and strain (as shown in references (see [36, 37])).

Spatial-temporal evolution of P_f and A_f , is determined from the coupled time-dependent LGD type Euler-Lagrange equations, derived by minimizing the system's free energy F :

$$\Gamma_P \frac{\partial P_f}{\partial t} + a_P P_f + b_P P_f^3 + \eta A_f^2 P_f - g \Delta P_f = E_f, \quad (3a)$$

$$\Gamma_A \frac{\partial A_f}{\partial t} + a_A A_f + b_A A_f^3 + \eta P_f^2 A_f - g \Delta A_f = 0, \quad (3b)$$

where Γ_P and Γ_A are Landau-Khalatnikov relaxation coefficients, and g is a positive gradient coefficient written in an isotropic approximation. The relaxation times of P_f and A_f are $\tau_P = \Gamma_P/|a_P|$ and $\tau_A = \Gamma_A/|a_A|$, respectively. The corresponding boundary conditions for (3) are of the third kind [38]:

$$\left(P_f + \Lambda_P \frac{\partial P_f}{\partial n} \right) \Big|_S = 0, \quad \left(A_f + \Lambda_A \frac{\partial A_f}{\partial n} \right) \Big|_S = 0. \quad (4)$$

Here $\Lambda_P = \frac{g}{c_P}$ and $\Lambda_A = \frac{g}{c_A}$ are extrapolation lengths, which physical range is (0.5 – 5) nm [39]. Here S is the surface of the HfO_{2-y} nanoparticle.

Examples of how the effective LGD model works quantitatively are given in Refs.[29 - 31]. There polarization hysteresis loops, measured experimentally in $\text{Hf}_x\text{Zr}_{1-x}\text{O}_2$ thin films by Park et al. [9], are shown. The LGD-model parameters, determined from fitting of experimental results from Park et al. [9] in the references .[29 - 31], are listed in the last four columns of **Table II**.

Table II. Landau-Ginsburg-Devonshire parameters of $\text{Hf}_x\text{Zr}_{1-x}\text{O}_2$ films*

x	phase	$P_r(x)$, C/m ²	$P_{c1,2}(x)$, C/m ²	$\tilde{\chi}(x)$	$a_P(x)$ $\times 10^9$, m/F	$a_A(x)$ $\times 10^9$, m/F	$b_P \approx b_A$ $\times 10^{10}$, Vm ⁵ /C ³	$\eta(x)$ $\times 10^{10}$, Vm ⁵ /C ³
0	PE	0	N/A	35	3.227	N/P	N/P	N/P
0.2	AFE	0	0.22, 0.17	40	0.812	-0.936	0.9	1.93
0.3	AFE	0	0.22, 0.15	50	0.010	-1.190	1.3	2.458
0.4	AFE	0	0.18, 0.11	48	-0.104	-0.937	1.1	2.888
0.50	FE	0.195	N/A	95	-0.594	N/P	1.563	N/P
0.57	FE	0.173	N/A	76	-0.743	N/P	2.483	N/P
0.70	FE	0.038	N/A	400	-0.141	N/P	10.039	N/P
0.81	PE	0.025	N/A	31	3.643	N/P	N/P	N/P
1.00	PE	0	N/A	19	5.944	N/P	N/P	N/P
h	films with thickness $h = 9.2$ nm							

*The content of Table I is licensed under a Creative Commons Attribution (CC BY) license

(<https://creativecommons.org/licenses/by/4.0/>) in Supplementary Information to Ref.

(<https://doi.org/10.1063/5.0209123>)

B. Density Functional Theory calculations

Calculations were made using density functional theory, which allows us to calculate the parameters of the ground state structure by minimizing the total energy functional. The functional is not exactly known, and the result depends on its model form. The calculations were performed using the full-electron package FPLO (full potential local orbital) for the local density approximation (LDA) and generalized gradient approximation (GGA) functionals, and the FPLO basis was used. A 12-atom hafnium oxide supercell was simulated for crystalline phases of different symmetries, with a $6 \times 6 \times 6$ grid of Brillouin zone k-points. The equilibrium lattice parameters were found and compared with experimental data and values determined using other calculation packages. For both functionals, we confirmed that the crystal structure with monoclinic symmetry has the lowest ground state energy in the bulk HfO₂. At the same time, the difference between the energies of the polar orthorhombic phase (shown in **Fig. 1(b)**) and monoclinic phase (shown in **Fig. 1(a)**) calculated in HfO₂ structure by the LDA and GGA approximations turned out to be smaller (~30 eV) than that calculated by other calculation methods.

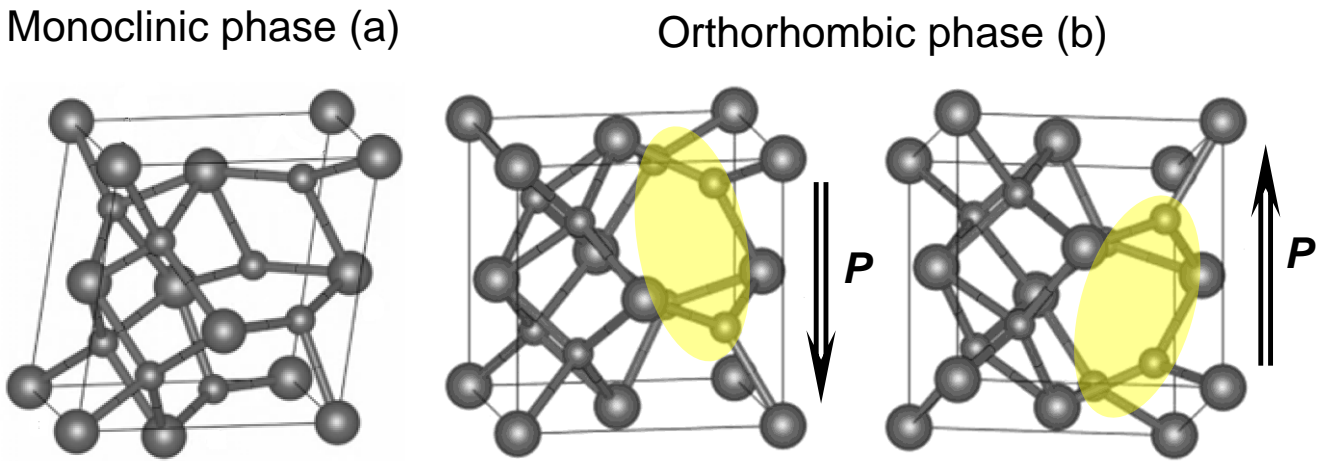


Figure 1. The HfO_2 structure with nonpolar monoclinic symmetry (a) and polar orthorhombic symmetry (b). The polarization of the orthorhombic phase can be visualized as a shift of four oxygen atoms (shown by yellow area) along z-direction. Adapted from Ref. [40]

Thus, the DFT calculations reveal that small HfO_2 nanoparticles may become polar, especially in the presence of impurity atoms and/or oxygen vacancies.

EXPERIMENTAL VERIFICATION

A. X-ray diffraction spectra of the oxygen-deficient HfO_{2-y} nanoparticles

To verify the model, we prepared several sample groups of stoichiometric HfO_2 , oxygen-deficient HfO_{2-y} and HfO_{2-y} doped nanoparticles doped with Y. Namely:

- **Sample group 1** annealed at 700°C for 6 hours (or more) in air,
- **Sample group 2** annealed at 600°C for 6 hours in air + 3,8 mol% of Y_2O_3 ,
- **Sample group 3** annealed at 500°C for 6 hours in $\text{CO}+\text{CO}_2$.

This diverse approach yielded samples with distinct color variations, reflecting differences in their oxygen vacancy concentrations, namely for Samples from 1 to 3 color changed from white to dark grey. The average size of the nanoparticles (20 nm) was determined from TEM.

X-ray diffraction (XRD) analysis using an XRD-6000 diffractometer with $\text{Cu-K}\alpha 1$ radiation ($2\theta = 15-70^\circ$) and the database of the International Committee for Powder Diffraction Standards (JCPDS PDF-2) was used for identification the crystallographic phases of the HfO_2 nanoparticles. In the result, we confirmed the coexistence of both monoclinic and ferroelectric-like orthorhombic phases inside the oxygen-deficient nanoparticles. Namely, its significant amount has been found in sample groups 2 and 3 (see **Table III**). Notably, the relative abundance of each phase exhibited a demonstrably shifting pattern based on the specific annealing protocol employed, highlighting the sensitivity of phase composition to processing parameters.

Table III. XRD studies of HfO_{2-y} nanopowder sample groups

Sample group №	Phase	Mass fraction, %	Scattering region sizes, nm	Lattice parameters		
				<i>a</i> , Å	<i>b</i> , Å	<i>c</i> , Å
1	m	100	13	5,1220	5,1603	5,3025
2	m	16,85	11	5,1408	5,1771	5,4113
	o	83,15	7	10,1180	5,1353	5,1583
3	m	13,24	12	5,1250	5,1580	5,3048
	o	86,76	8	10,1089	5,2076	5,1202

XRD analysis revealed a progressive shift in the sample's phases with changing annealing conditions. A Sample group 1 has the pure monoclinic phase ("m") as should be for a stoichiometric HfO₂ nanopowder. The fraction of non-ferroelectric monoclinic phase ("m") decreased from 100% (for the sample group 1) to 13.24% (for the sample group 3), while the ferroelectric-like orthorhombic phase ("o") increased from 0% (for the sample group 1) to 86.76% (for the sample group 3), respectively. The progressive change in the phase composition, namely increasing of the ferroelectric-like orthorhombic phases, is attributed to the rise in oxygen vacancy concentration induced by the specific annealing conditions and/or rare-earth doping. Corresponding XRD spectra of oxygen-deficient HfO_{2-y} nanopowders are shown in **Fig. 2** and **Fig. 3**, respectively.

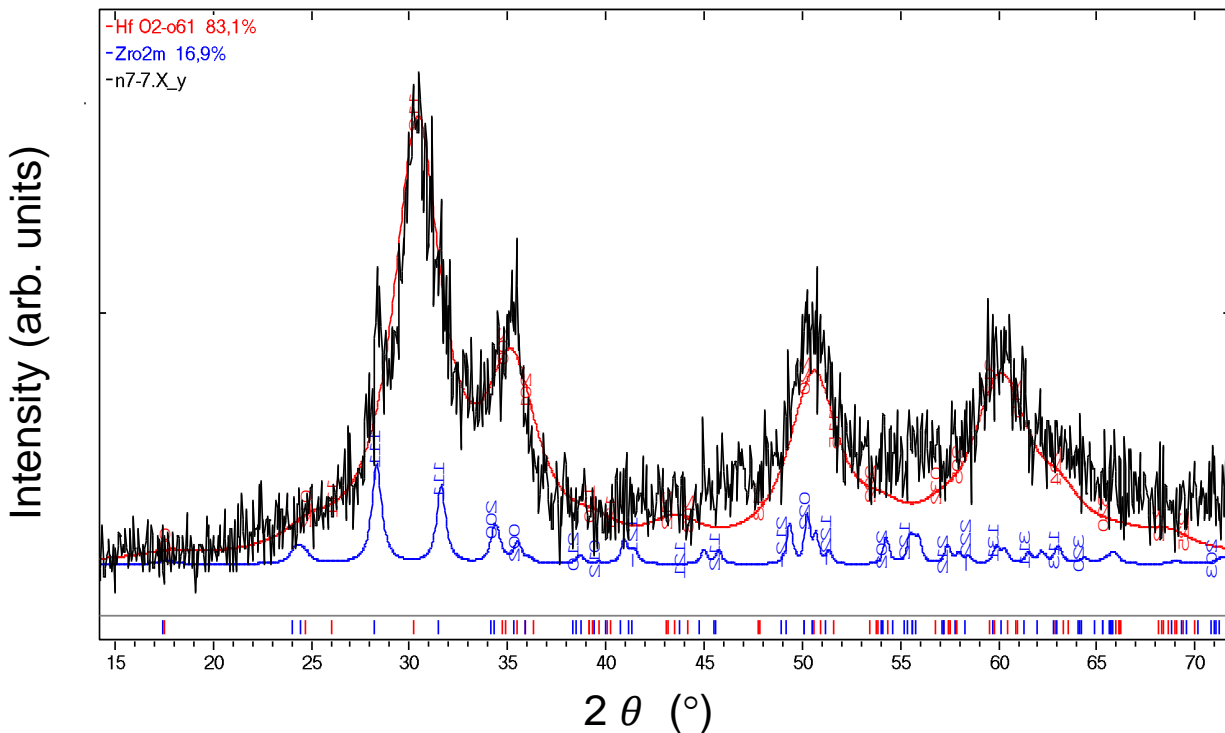


Figure 2. XRD spectra of oxygen-deficient HfO_{2-y} nanopowders annealed at 600°C for 6 hours in air under the presence of 3,8 mol% of Y₂O₃

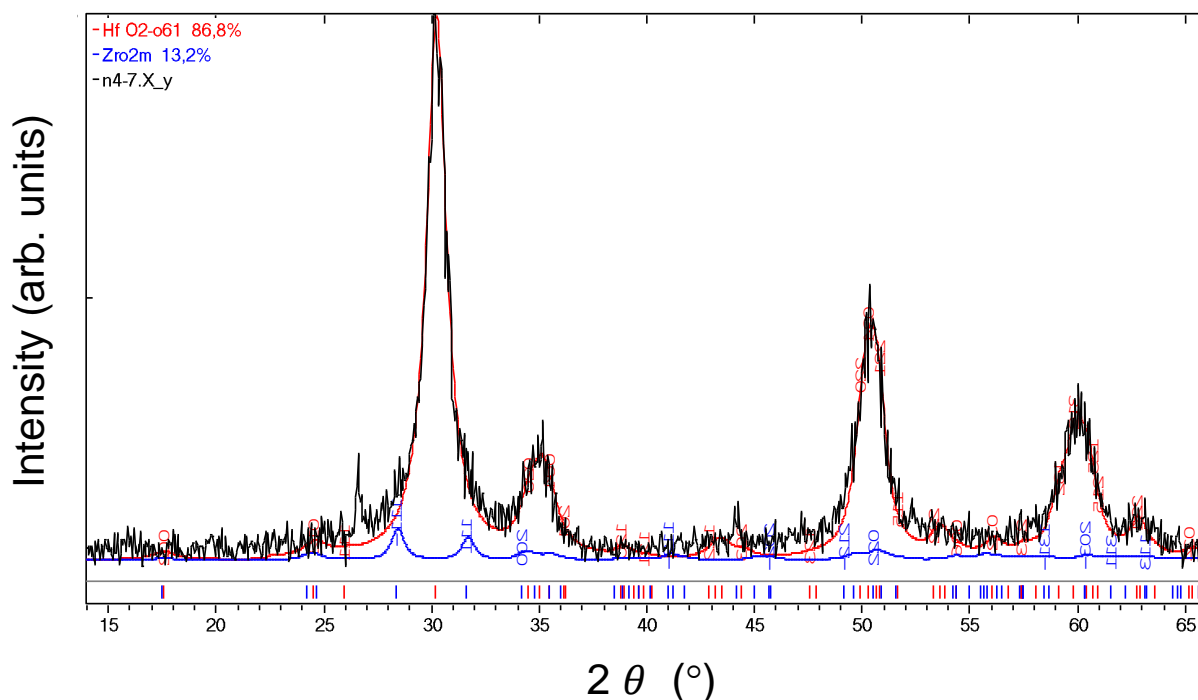


Figure 3. XRD spectra of oxygen-deficient HfO_{2-y} nanopowders annealed at 500°C for 6 hours in $\text{CO}+\text{CO}_2$ atmosphere

This comprehensive dataset, along with the sizes of the coherent scattering regions, forms foundation for the subsequent verification of the proposed effective Landau-Ginzburg-Devonshire (LGD) model.

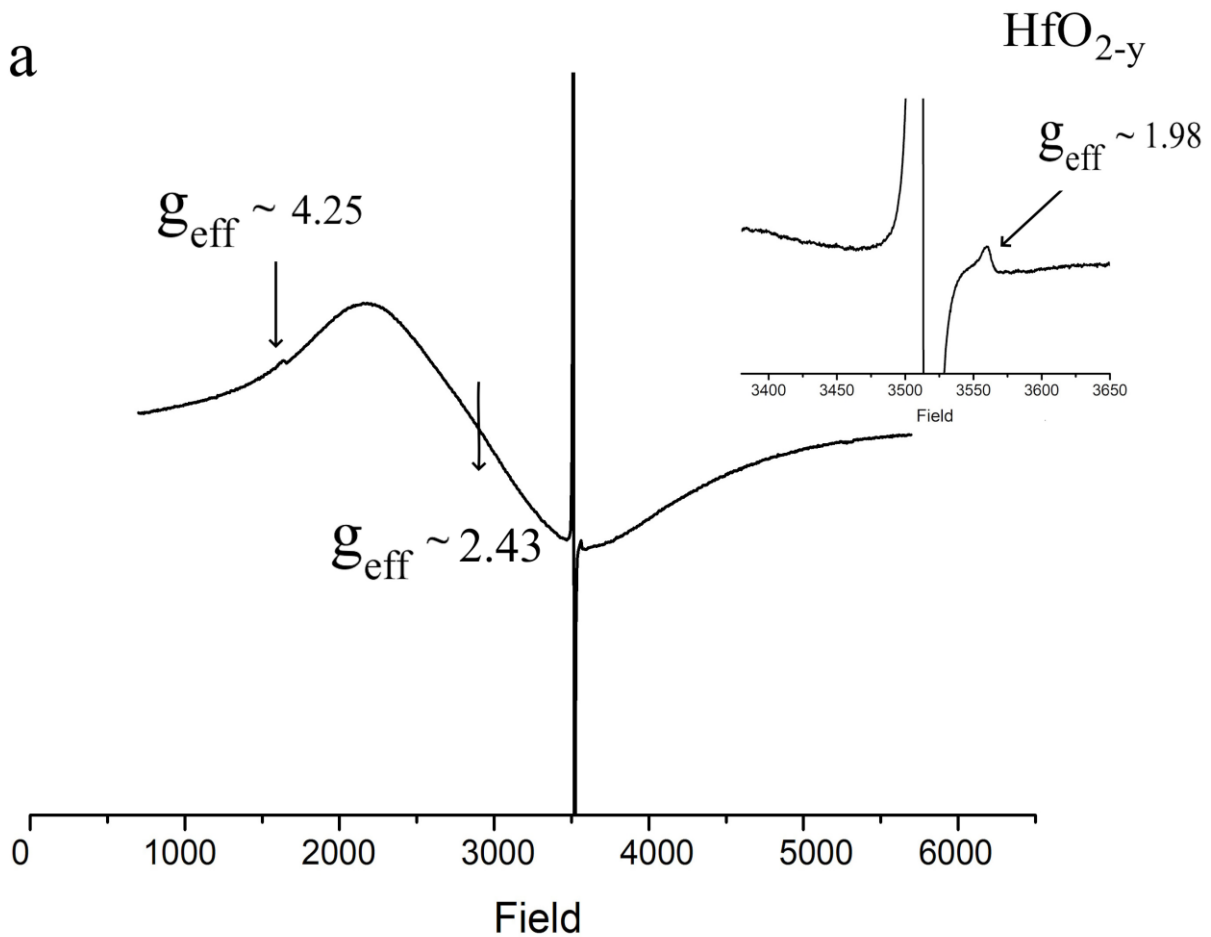
B. EPR spectra the oxygen-deficient HfO_{2-y} nanoparticles

EPR measurements were carried out on X-band Bruker Elexsys E580 spectrometer operating at 9.8 GHz frequency at room temperature. The EPR spectra of HfO_{2-y} and $\text{HfO}_{2+3,8}$ mol% of Y_2O_3 nanoparticles are presented in **Fig. 4**. The Y^{3+} and Hf^{4+} ions have a closed electron shell and do not contribute to the observed EPR spectra, therefore the spectral line may be due to impurities present in the studied samples, charged oxygen vacancies or Y^{2+} , Hf^{3+} cations that have lowered their valence state due to the formation of oxygen vacancies.

The sharp intense line in **Fig. 4(a)** belongs to organic radicals present in the sample annealed in a $\text{CO}+\text{CO}_2$ atmosphere, while the weak signal with $g_{\text{eff}} \sim 4.25$ is characteristic of Fe^{3+} impurities. Much more interesting is the line with $g_{\text{eff}} \sim 1.98$ shown in the inset on **Fig. 4(a)**. This line, according to Ref.[41], can be attributed to Hf^{3+} ion associated with an oxygen vacancy. The sharp, well-shaped signal apparently corresponds to Hf in the bulk of the sample, which is not affected by defects present on the surface of the nanoparticles. On the other hand, Hf^{3+} located in the near-surface layer should give a broad line due to the

distribution of parameters that determine the shape of the EPR line. Thus, the line with $g_{\text{eff}} \sim 2.43$ may belong to a large near-surface layer abundant in oxygen vacancies and Hf^{3+} cations.

The entire spectrum shown in **Fig. 4(b)** has a very weak intensity. Its true magnitude can be estimated from the signal associated with the Fe^{3+} impurity, whose intensity is close to the appropriate signal in **Fig. 4(a)**. The broad line centered at $g_{\text{eff}} \sim 2.2$ can be described as a superposition of at least two wide lines. This line can be associated with the presence of the Y^{2+} ion [42] the EPR parameters of which are affected by surface defects. However, there is a significant difference from the values of the EPR parameters given in the mentioned work. Moreover, annealing in an oxygen atmosphere makes the formation of Y^{2+} ions very unlikely. Thus, the nature of this line in the EPR spectrum requires further detailed study.



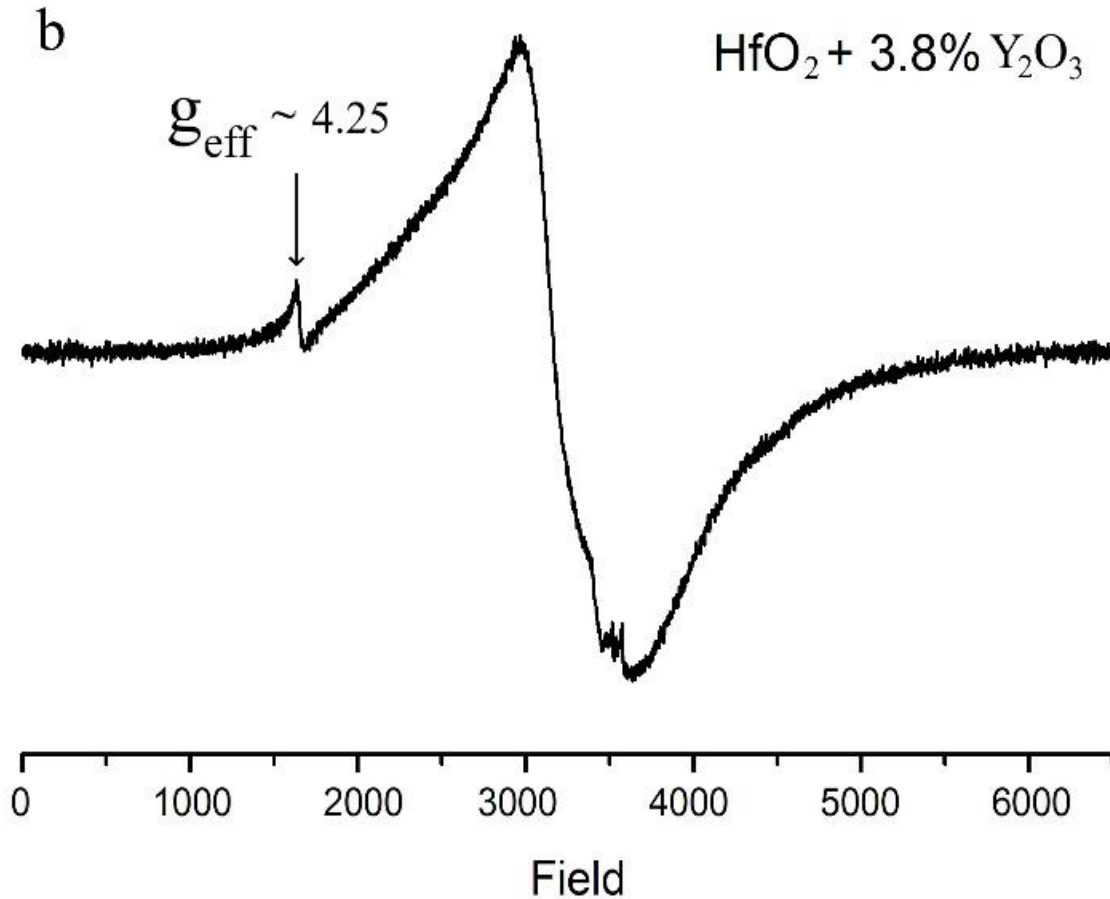


Figure 4. EPR spectra of oxygen-deficient HfO_{2-y} nanopowders annealed at 500°C for 6 hours in $\text{CO}+\text{CO}_2$ atmosphere (**a**) and $\text{HfO}_2+3,8$ mol% of Y_2O_3 nanoparticles annealed at 600°C for 6 hours in air (**b**).

EFFECTIVE LGD MODEL FOR OXYGEN-DEFICIENT HfO_{2-y} NANOPARTICLES

Using the phase fractions and coherent scattering region sizes obtained from XRD (**Table III**), we employ the effective LGD model to simulate stoichiometric and oxygen-deficient HfO_2 nanoparticles. The model incorporates a vacancy concentration gradient, mimicking the presumed distribution, as shown in **Fig. 5(a)**.

These vacancies act as elastic dipoles, influencing the material's stability. The calculated polarization-field hysteresis loops (shown in **Fig. 5(b)**) reveal a progressive transition from dielectric-like to antiferroelectric and ferroelectric characteristics with increasing vacancy concentration, aligning well with the experimental XRD findings.

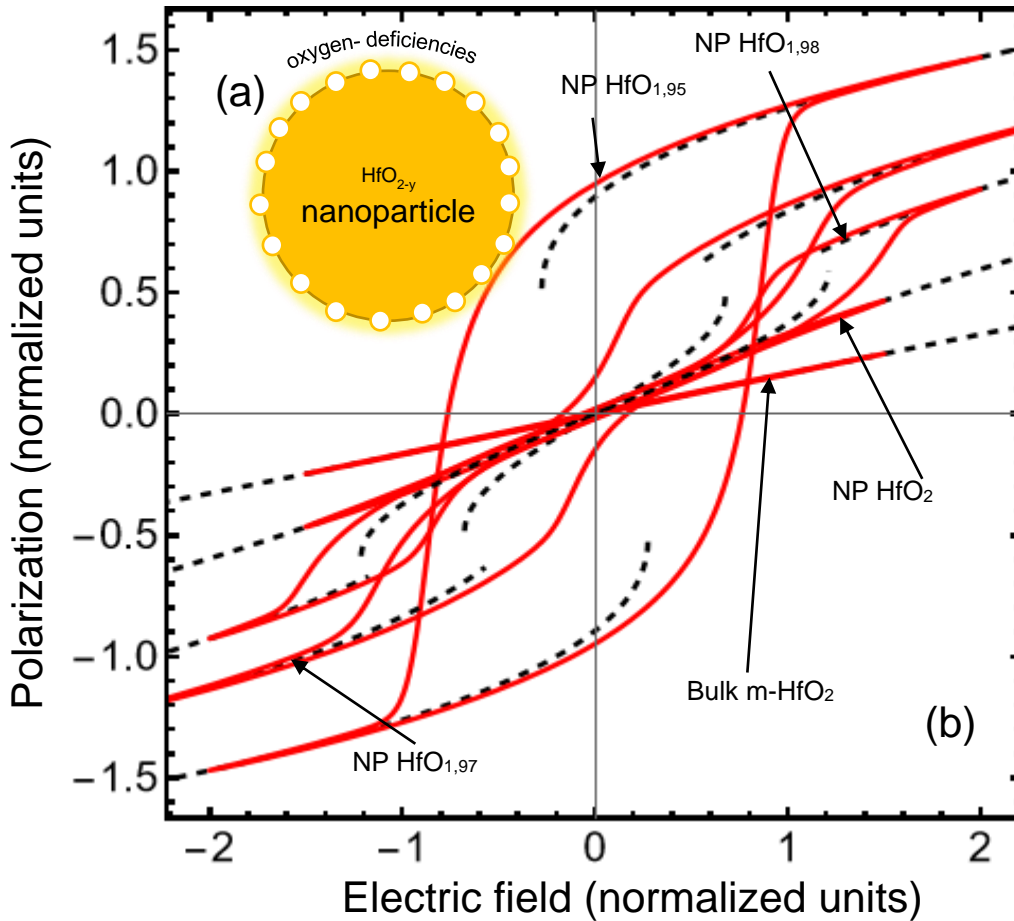


Figure 5. (a) The radial cross-section of the oxygen-deficient HfO_{2-y} nanoparticle. (b) Polarization-field dependences (hysteresis loops) calculated using the effective LGD model for the stoichiometric HfO_2 bulk, 20-nm size stoichiometric HfO_2 nanoparticles (NP) and HfO_{2-y} nanoparticles with different concentration of oxygen vacancies near the surface: $y = 2\%$, 3% and 5% . The dielectric-type, paraelectric-type, antiferroelectric-type and ferroelectric-type loops are shown. Black dotted curves show the equilibrium polarization-field dependences and red solid curves show the dynamic polarization-field hysteresis loops.

CONCLUSIONS

Obtained results indicate the strong correlation between the crystalline structure symmetry, point defects and possible appearance of the ferroelectric-like polarization in HfO_{2-y} nanoparticles. Notably, that XRD and EPR analysis revealed the formation of the ferroelectric-like orthorhombic phase in the oxygen-deficient HfO_{2-y} nanoparticles (both in pure and doped with rare-earth element yttrium). Also, DFT calculations showed that small HfO_2 nanoparticles may become polar, especially in the presence of impurity atoms and/or oxygen vacancies.

To explain the experimental results, we have modified the effective LGD model [29-31] through a tailored parameterization approach, specifically focusing on the Landau expansion coefficients associated with polar (FE) and antipolar (AFE) orderings, which agrees with the performed DFT calculations. The effective LGD model can be useful for the development of the novel generation of silicon-compatible ferroelectric nanomaterials based on the $\text{Hf}_x\text{Zr}_{1-x}\text{O}_{2-y}$.

The combined experimental and theoretical approach has potential for the field of nanotechnology and material science.

Authors' contribution

The research idea belongs to E.A.E., A.N.M. and Y.O.Z. E.A.E. wrote the codes, performed numerical calculations and compared their results to experiments. I.V.K. performed DFT calculations. Y.O.Z. performed EPR measurements. O.V.L., V.N.P., L.P.Y., prepared the samples. M.V.K. and performed XRD measurements. A.N.M. and H.V.S. wrote the manuscript draft. All co-authors discussed the results.

Acknowledgment

The work of E.A.E., I.V.K., Y.O.Z. and L.P.Y. are funded by the National Research Foundation of Ukraine (project "Silicon-compatible ferroelectric nanocomposites for electronics and sensors", grant N 2023.03/0127). The work of A.N.M. is supported by the Ministry of Science and Education of Ukraine (grant № PH/ 23 - 2023, "Influence of size effects on the electrophysical properties of graphene-ferroelectric nanostructures") at the expense of the external aid instrument of the European Union for the fulfillment of Ukraine's obligations in the Framework Program of the European Union for scientific research and innovation "Horizon 2020".

REFERENCES

-
- 1 T. Mikolajick, S. Slesazeck, H. Mulaosmanovic, M. H. Park, S. Fichtner, P. D. Lomenzo, M. Hoffmann, U. Schroeder. Next generation ferroelectric materials for semiconductor process integration and their applications, *J. Appl. Phys.* 129, 100901 (2021), <https://doi.org/10.1063/5.0037617>
 - 2 K.-H. Kim, I. Karpov, R. H. Olsson III, D. Jariwala. Wurtzite and fluorite ferroelectric materials for electronic memory, *Nature Nanotechnology* 18, 422 (2023). <https://doi.org/10.1038/s41565-023-01361-y>
 - 3 W. Yang, C. Yu, H. Li, M. Fan, X. Song, H. Ma, Z. Zhou, P. Chang, P. Huang, F. Liu, X. Liu, J. Kang. Ferroelectricity of hafnium oxide-based materials: Current statuses and future prospects from physical mechanisms to device applications. *Journal of Semiconductors* 44, 053101 (2023), <https://doi.org/10.1088/1674-4926/44/5/053101>

-
- 4 G. A. Kourouklis, and E. Liarokapis. Pressure and temperature dependence of the Raman spectra of zirconia and hafnia. *Journal of the American Ceramic Society* 74, 520 (1991), <https://doi.org/10.1111/j.1151-2916.1991.tb04054.x>
- 5 M. Ishigame, and T. Sakurai. Temperature dependence of the Raman spectra of ZrO₂. *Journal of the American Ceramic Society* 60, 367 (1977), <https://doi.org/10.1111/j.1151-2916.1977.tb15561.x>
- 6 T.S. Boscke, S. Teichert, D. Brauhaus, J. Muller, U. Schroder, U. Bottger, and T. Mikolajick, Phase transitions in ferroelectric silicon doped hafnium oxide, *Appl. Phys. Lett.* 99, 112904 (2011), <https://doi.org/10.1063/1.3636434>.
- 7 Yu Yun, P. Buragohain, M. Li, Z. Ahmadi, Y. Zhang, X. Li, H. Wang, J. Li, P. Lu, L. Tao, H. Wang, Intrinsic ferroelectricity in Y-doped HfO₂ thin films, *Nature Materials*, 21, 903 (2022), <https://doi.org/10.1038/s41563-022-01282-6>
- 8 F. Delodovici, P. Barone, and S. Picozzi. Finite-size effects on ferroelectricity in rhombohedral HfO₂. *Phys. Rev. B* 106, 115438 (2022), <https://doi.org/10.1103/PhysRevB.106.115438>
- 9 M. H. Park, Y. H. Lee, H. J. Kim, T. Schenk, W. Lee, K. Do Kim, F. P. G. Fengler, T. Mikolajick, U. Schroeder, and C. S. Hwang. Surface and grain boundary energy as the key enabler of ferroelectricity in nanoscale hafnia-zirconia: a comparison of model and experiment. *Nanoscale* 9, 9973 (2017), <https://doi.org/10.1039/C7NR02121F>
- 10 D. Hyun Lee, Y. Lee, K. Yang, J.Y. Park, S.H. Kim, P.R.S. Reddy, M. Materano, H. Mulaosmanovic, T. Mikolajick, J.L. Jones, U. Schroeder, M.H. Park, Domains and domain dynamics in fluorite-structured ferroelectrics *Appl. Phys. Rev.* 8, 021312 (2021), <https://doi.org/10.1063/5.0047977>
- 11 L.-Y. Ma and S. Liu. Structural Polymorphism Kinetics Promoted by Charged Oxygen Vacancies in HfO₂ *Phys. Rev. Lett.* 130, 096801 (2023), <https://doi.org/10.1103/PhysRevLett.130.096801>
- 12 M.D. Glinchuk, A.N. Morozovska, A. Lukowiak, W. Stręk, M.V. Silibin, D.V. Karpinsky, Y. Kim, and S.V. Kalinin.. Possible Electrochemical Origin of Ferroelectricity in HfO₂ Thin Films. *Journal of Alloys and Compounds*, 830, 153628 (2020), <https://doi.org/10.1016/j.jallcom.2019.153628>
- 13 S. Kang, W.-S. Jang, A. N. Morozovska, O. Kwon, Y. Jin, Y.H. Kim, H. Bae, C. Wang, S.H. Yang, A. Belianinov, and S. Randolph, Highly enhanced ferroelectricity in HfO₂-based ferroelectric thin film by light ion bombardment. *Science*, 376, 731-738 (2022), <https://doi.org/10.1126/science.abk3195>
- 14 W. Yang, C. Yu, H. Li, M. Fan, X. Song, H. Ma, Z. Zhou, P. Chang, P. Huang, F. Liu, X. Liu, J. Kang. Ferroelectricity of hafnium oxide based materials: Current statuses and future prospects from physical mechanisms to device applications. *Journal of Semiconductors* 44, 1-45 (2023), <https://doi.org/10.1088/1674-4926/44/5/053101>
- 15 M. H. Park, C.-C. Chung, T. Schenk, C. Richter, K. Opsomer, C. Detavernier, C. Adelman, J.L. Jones, T. Mikolajick, U. Schroeder. Effect of Annealing Ferroelectric HfO₂ Thin Films: In Situ, High

-
- Temperature X-Ray Diffraction. *Advanced Electronic Materials* **4**, 1800091 (2018), <https://doi.org/10.1002/aelm.201800091>
- 16 K. P. Kelley, A. N. Morozovska, E. A. Eliseev, Y. Liu, S. S. Fields, S. T. Jaszewski, T. Mimura, J. F. Ihlefeld, S. V. Kalinin. Ferroelectricity in Hafnia Controlled via Surface Electrochemical State. *Nature Materials* **22**, 1144 (2023) <https://doi.org/10.1038/s41563-023-01619-9>
- ¹⁷ J. Tang, J. Fabbri, R. D. Robinson, Y. Zhu, I. P. Herman, M. L. Steigerwald, and L. E. Brus. Solid-Solution Nanoparticles: Use of a Nonhydrolytic Sol–Gel Synthesis to Prepare HfO₂ and Hf_xZr_{1-x}O₂ Nanocrystals. *Chemistry of materials* **16**, 1336, (2004), <https://doi.org/10.1021/cm049945w>
- ¹⁸ H. P. Kumar, S. Vidya, S. S. Kumar, C. Vijayakumard, S. Solomon, J.K. Thomas. Optical properties of nanocrystalline HfO₂ synthesized by an auto-igniting combustion synthesis. *Journal of Asian Ceramic Societies* **3**, 64–69 (2015), <http://dx.doi.org/10.1016/j.jascer.2014.10.009>
- ¹⁹ V. Jayaraman, G. Bhavesh, S. Chinnathambi, S. Ganesan, and P. Aruna. Synthesis and characterization of hafnium oxide nanoparticles for bio-safety. *Materials Express* **4**, 375 (2014), <https://doi.org/10.1166/mex.2014.1190>
- ²⁰ Y. Wan, and X. Zhou. Formation mechanism of hafnium oxide nanoparticles by a hydrothermal route. *RSC advances* **7**, 7763 (2017), <https://doi.org/10.1039/C6RA26663K>
- ²¹ L. Ren, L. Yang, S. Zhang, H. Li, Y. Zhou, D. Ai, Zongliang Xie et al. Largely enhanced dielectric properties of polymer composites with HfO₂ nanoparticles for high-temperature film capacitors. *Composites Science and Technology* **201**, 108528 (2021), <https://doi.org/10.1016/j.compscitech.2020.108528>
- ²² T. L. McGinnity, V. Sokolova, O. Prymak, P. D. Nallathamby, M. Epple, and R. K. Roeder. Colloidal stability, cytotoxicity, and cellular uptake of HfO₂ nanoparticles. *Journal of Biomedical Materials Research Part B: Applied Biomaterials* **109**, 1407 (2021), <https://doi.org/10.1002/jbm.b.34800>
- ²³ S. Kumar, T. Dehury, and C. Rath. Stabilization of Cubic Phase at Room Temperature and Photoluminescence Properties of Dy and Sm Co-Doped HfO₂ Nanoparticles. *ECS Journal of Solid State Science and Technology*, **10**, 081009 (2021), <https://doi.org/10.1149/2162-8777/ac1c54>
- ²⁴ Eugene A. Eliseev, Yuri O. Zagorodniy, Victor N. Pavlikov, Oksana V. Leshchenko, Hanna V. Shevilakova, Miroslav V. Karpec, Andrei D. Yaremkevych, Olena M. Fesenko, Sergei V. Kalinin, and Anna N. Morozovska. Phase diagrams and polarization reversal in nanosized Hf_xZr_{1-x}O_{2-y}. *AIP Advances*, **14**, 055224 (2024), <https://doi.org/10.1063/5.0209123>
- ²⁵ K. Laganovska, V. Vitola, E. Einbergs, I. Bite, A. Zolotarjovs, M. Leimane, G. Tunens, and K. Smits. "Impact of Europium and Niobium Doping on Hafnium Oxide (HfO₂): Comparative Analysis of Sol–Gel and Combustion Synthesis Methods." *Ceramics*, **7**, 15–28 (2024), <https://doi.org/10.3390/ceramics7010002>

-
- ²⁶ Konomi Fujimoto, Yukio Sato, Yoshifumi Fuchikami, Ryo Teranishi, and Kenji Kaneko. "Orthorhombic-like atomic arrangement in hafnium-oxide-based nanoparticles." *Journal of the American Ceramic Society* 105, 2823-2831 (2022). <https://doi.org/10.1111/jace.18242>
- ²⁷ M. H. Park, C.-C. Chung, T. Schenk, C. Richter, K. Opsomer, C. Detavernier, C. Adelman, J.L. Jones, T. Mikolajick, U. Schroeder. Effect of Annealing Ferroelectric HfO₂ Thin Films: In Situ, High Temperature X-Ray Diffraction. *Advanced Electronic Materials* 4, 1800091 (2018), <https://doi.org/10.1002/aelm.201800091>
- ²⁸ K. P. Kelley, A. N. Morozovska, E. A. Eliseev, Y. Liu, S. S. Fields, S. T. Jaszewski, T. Mimura, J. F. Ihlefeld, S. V. Kalinin. Ferroelectricity in Hafnia Controlled via Surface Electrochemical State. *Nature Materials* 22, 1144 (2023) <https://doi.org/10.1038/s41563-023-01619-9>
- 29 A. N. Morozovska, M. V. Strikha, K. P. Kelley, S. V. Kalinin, and E. A. Eliseev. Effective Landau-type model of a HfxZr1-xO2-graphene nanostructure, *Phys. Rev. Applied* 20, 054007 (2023) <https://doi.org/10.1103/PhysRevApplied.20.054007>
- 30 E. A. Eliseev, Y. O. Zagorodniy, V. N. Pavlikov, O. V. Leshchenko, H. V. Shevilakova, M. V. Karpec, A. D. Yaremkevych, O. M. Fesenko, S. V. Kalinin, and A. N. Morozovska. Phase diagrams and polarization reversal in nanosized HfxZr1-xO2-y, *AIP Advances*, 14, 055224 (2024), <https://doi.org/10.1063/5.0209123>
- 31 E. A. Eliseev, S. V. Kalinin, A. N. Morozovska. Ferro-ionic States and Domains Morphology in HfxZr1-xO2 Nanoparticles (2024), <https://doi.org/10.48550/arXiv.2410.04476>
- 32 R. Blinc, B. Zeks, *Soft Mode in Ferroelectrics and Antiferroelectrics*; North-Holland Publishing Company, Amsterdam, Oxford, 1974.
- 33 A. K. Tagantsev, K. Vaideeswaran, S. B. Vakhrushev, A. V. Filimonov, R. G. Burkovsky, A. Shaganov, D. Andronikova, A. I. Rudskoy, A. Q. R. Baron, H. Uchiyama, D. Chernyshov, A. Bosak, Z. Ujma, K. Roleder, A. Majchrowski, J.-H. Ko & N. Setter. The Origin of Antiferroelectricity in PbZrO₃. *Nature Commun.* 4, article number: 2229 (2013), <https://doi.org/10.1038/ncomms3229>.
- 34 K.M. Rabe, Antiferroelectricity in Oxides: A Reexamination. In *Functional Metal Oxides*; John Wiley & Sons, Ltd; pp 221–244. <https://doi.org/10.1002/9783527654864.ch7> .
- 35 J. Hlinka, T. Ostapchuk, E. Buixaderas, C. Kadlec, P. Kuzel, I. Gregora, J. Kroupa, M. Savinov, A. Klic, J. Drahoš, I. Etxebarria, and J. Dec. Multiple Soft-Mode Vibrations of Lead Zirconate. *Phys. Rev. Lett.* 112, 197601 (2014). <https://doi.org/10.1103/PhysRevLett.112.197601>.
- 36 A. Tagantsev, L.E. Cross, J. Fousek, *Domains in Ferroic Crystals and Thin Films*; Springer: New York, 2010. 10.1007/978-1-4419-1417-0

-
- 37 A. Kvasov and A.K. Tagantsev. Role of high-order electromechanical coupling terms in thermodynamics of ferroelectric thin films. *Phys. Rev. B* 87, 184101 (2013), <https://doi.org/10.1103/PhysRevB.87.184101>.
- 38 R. Kretschmer and K.Binder. "Surface effects on phase transitions in ferroelectrics and dipolar magnets." *Phys. Rev. B* 20, 1065 (1979), <https://doi.org/10.1103/PhysRevB.20.1065>.
- 39 Chun-Lin Jia, Valanoor Nagarajan, Jia-Qing He, Lothar Houben, Tong Zhao, Ramamoorthy Ramesh, Knut Urban & Rainer Waser, "Unit-cell scale mapping of ferroelectricity and tetragonality in epitaxial ultrathin ferroelectric films." *Nature Materials* 6, 64 (2007), <https://doi.org/10.1038/nmat1808>.
- ⁴⁰ R. Materlik, C. Künneth, and A. Kersch. The origin of ferroelectricity in $\text{Hf}_{1-x}\text{Zr}_x\text{O}_2$: A computational investigation and a surface energy model, *J. Appl. Phys.* 117, 134109 (2015), <http://dx.doi.org/10.1063/1.4916707>
- 41 S. Wright, R. C. Barklie, EPR characterization of defects in $m\text{-HfO}_2$, *J Mater Sci: Mater Electron* (2007) 18:743–746 DOI 10.1007/s10854-007-9119-6
- 42 M. Fang, D. S. Lee, J. W. Ziller, R. J. Doedens, J. E. Bates, F. Furche, W. J. Evans, Synthesis of the $(\text{N}_2)_3$ -Radical from Y^{2+} and Its Protonolysis Reactivity To Form $(\text{N}_2\text{H}_2)_2^-$ via the $\text{Y}[\text{N}(\text{SiMe}_3)_2]_3/\text{KC}_8$ Reduction System, *J. Am. Chem. Soc.* 2011, 133, 11, 3784–3787, <https://doi.org/10.1021/ja1116827>